

Controlled One-Step Synthesis of Nanocrystalline Anatase and Rutile TiO₂ Powders by In-Flight Thermal Plasma Oxidation

Ya-Li Li and Takamasa Ishigaki*

National Institute for Materials Science, Advanced Materials Laboratory, Tsukuba, Ibaraki 305-0044, Japan

Received: April 28, 2004; In Final Form: July 7, 2004

Highly crystallized TiO₂ nanocrystallites (10–50 nm in size) with controlled phase structures (anatase and rutile) were synthesized using a one-step process. Flying TiC micrometer-size powder was oxidized in Ar–O₂ and Ar–H₂–CO₂ plasmas with various configurations used for injecting oxygen into the reaction system. The oxide nanocrystallites formed were characterized by X-ray diffractometry, Raman spectroscopy, and high-resolution transmission electron microscopy. The TiO₂ nanocrystallites formed in the Ar–O₂ plasma consisted of isolated single-crystal particles of anatase with spherical shapes and rutile grains crystallized in a hexagonal morphology. The fraction of anatase increased greatly with the oxygen flow rate in the Ar–O₂ plasma. On the other hand, oxidation of the carbide in the Ar–H₂–CO₂ plasma gave exclusively pure rutile nanocrystallites, regardless of the CO₂ concentration. Injecting oxygen at the plasma tail greatly reduced the size of the nanocrystallites. These results suggest that both the size and the phase compositions of nanocrystalline TiO₂ can be controlled using this thermal plasma oxidation process.

Introduction

Extensive research is underway on the synthesis and processing of nanocrystalline materials because of their wide range of applications for improving material structures and functional properties and because of their attractive properties. In particular, nanocrystalline TiO₂ is attractive for such applications as photocatalysts,^{1–3} solar cells,^{4,5} membranes,^{6,7} sensors,^{8,9} and nanoceramics.^{10,11} The high efficiency of the photocatalysis of TiO₂ nanocrystallites, in combination with their structural and thermal stability, makes this material well suited for cleaning air, water, and soils and for degrading hazardous chemicals.^{12,13} These attractive applications have motivated a lot of current research on the synthesis and structural control of TiO₂ aimed at improving the material properties.^{14–20}

The size and the phase structure of TiO₂ nanocrystallites are two key factors affecting their structural and functional properties such as light scattering, electrical, sintering behavior, and catalytic activity.^{5,10,11,21–24} Nanocrystalline TiO₂ has a high photocatalysis efficiency because it provides a large specific surface area.^{22,24} The role of the phase structure in the photocatalysis remains unclear; while most studies have shown that anatase has better catalytic performance than rutile,^{21,25} one recent study showed the opposite.²³ The ambiguity was, to a great extent, due to the use of TiO₂ nanocrystallites with poorly controlled sizes and phase structures.

Most of the nanocrystalline TiO₂ currently used is synthesized by flame oxidation of titanium tetrachloride or related reactants or by the sol–gel process, which usually produces either amorphous or anatase-rich products.^{14–20,25–29} The nanocrystalline TiO₂ produced by flame oxidation generally contains a high proportion of small-grain crystallized anatase, mixed with a small fraction of larger grain rutile; the phase content of the rutile can be changed only in a limited range (<30 wt %), regardless of the synthesis conditions.^{27–29} Anatase can be

transformed into rutile by annealing at a high temperature (700–1200 °C), but unavoidable grain growth occurs concurrently with phase transformation at high temperature, leading to significantly increased grain sizes or interparticulate sintering.^{30–32} The sol–gel process usually produces as-synthesized products that are amorphous and need to be subsequently annealed in a routine heat treatment at an elevated temperature to form anatase or rutile or need to be annealed under hydrothermal conditions to suppress grain growth.^{33–35} Compared with anatase, uniform and fine-grained rutile seems to be more difficult to obtain directly using current synthesis techniques.²⁹

We have synthesized nanocrystalline TiO₂ with controlled phase compositions (anatase and rutile) and grain sizes using a one-step process, that is, by thermal plasma oxidation of in-flight titanium carbide micrometer-size powders in an aerosol reactor.³⁶ Thermal plasma synthesis in an aerosol flowing reactor is an established technique for synthesizing micro- or nanocrystallites of various oxides and refractory carbide and nitride by virtue of its extremely high temperatures (3000–10 000 K), rapid heating and cooling rates, high production yield, and technical simplicity.³⁷ Using this method, we synthesized highly crystalline TiO₂ microspheres by controlling the oxygen input in Ar–O₂ plasma.³⁸ Partial oxidation of TiC powder produced unique microscale core–shell TiC–TiO₂ composite particles,³⁹ in which the shell TiO₂ parts always consisted of the rutile phase.⁴⁰

We have now used this one-step process to form highly crystallized nanocrystalline TiO₂ using different plasma gases (Ar + O₂, Ar + He + O₂, and Ar + H₂ + CO₂) and by varying the gas composition and injection configuration to control the formation of anatase and rutile TiO₂ nanocrystallites of different shapes and sizes. The in-flight oxidation of titanium carbide emits a large amount of titanium oxide species into a vapor phase, which results in quite a high degree of supersaturation in a vapor phase. The high degree of supersaturation is one of the most important characteristics of the present processing. Through the present processing, the rate of vaporization in the

* Corresponding Author: Fax: +81-29-860-4701; Tel: +81-29-860-4659; E-mail: ISHIGAKI.Takamasa@nims.go.jp.

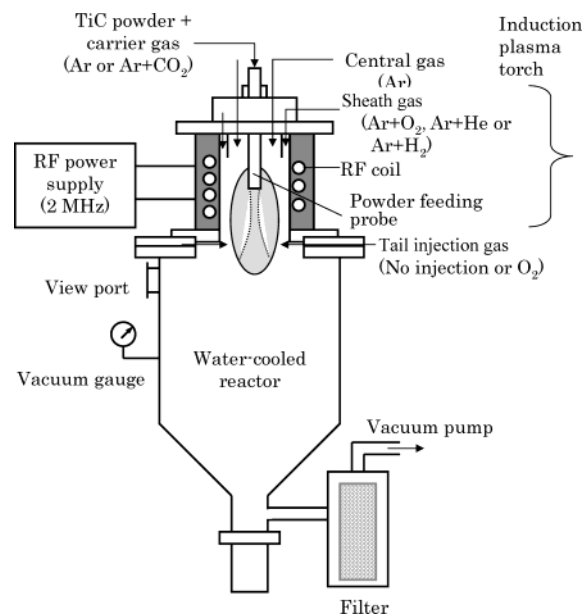


Figure 1. Schematic view of plasma-generating torch and plasma reactor for in-flight oxidation of TiC powder.

high-temperature plasma and the oxidation kinetics was balanced, thus giving nearly 100% TiO₂ products with controlled phase structures. The nanocrystallites produced were fully characterized by X-ray diffractometry, Raman spectroscopy, and high-resolution transmission electron microscopy (HRTEM).

Experimental Section

Synthesis. Nanocrystalline TiO₂ was synthesized by thermal plasma oxidation of flying TiC micro-powders in an aerosol flow reactor equipped with an induction plasma torch (Model PL-50, TEKNA Plasma Systems, Sherbrooke, Quebec, Canada). A schematic view of the plasma-generating torch and plasma reactor is shown in Figure 1. The reactor consists of a vertically oriented stainless steel cylinder (inner diameter: 250 mm) with a cone-shaped bottom connecting horizontally to a filter through a stainless steel outlet tube (diameter: 40 mm). The thermal plasma was generated in the induction-plasma torch connected with a radio frequency (RF) power-supply system (2 MHz, Nihon Koshuha Co. Ltd., Yokohama, Kanagawa, Japan).

The starting TiC powders were commercial products (TiC-M, Japan New Metals, Co., Ltd., Osaka, Japan), whose size distribution is described elsewhere,³⁸ with a particle diameter of 10–50 μm (mean: 28 μm ; standard deviation: 11 μm). The chemical composition was TiC_{0.97}, and the oxygen impurity content was measured to be 0.29 wt. %. The TiC particles were axially fed from the top of the plasma torch into the center of the plasma region by a powder-feeding probe using argon as a carrier. The plasma torch is described elsewhere.⁴¹

The plasma operating power was 25 or 40 kW, the powder feeding rate was 1.6–1.8 g/min, and the carrier gas flow rate was varied between 2.5 and 10 L/min. The pressure in the reaction chamber was 53–80 kPa. The plasma-generation and powder-feeding conditions are summarized in Table 1. Thermodynamic calculation showed that the TiO₂ tends to form a thermodynamically stable rutile phase under these gas and synthesis conditions.

The TiC powders were oxidized in Ar–O₂, Ar–He–O₂, and Ar–H₂–CO₂ plasmas. In the Ar–O₂ plasma treatment, oxygen (which is necessary for the oxidation of TiC) was mixed with argon and input from the top of the plasma torch as a sheath

gas. Adding diatomic gas to the argon increased the thermal conductivity, resulting in improved heat transfer from the plasma to the particles. The oxygen flow rates were 2.5, 5, 7.5, 10, 15, or 20 L/min, and the total flow rate of the sheath gases (Ar + O₂) was kept at 90 L/min. The flow rate of the argon at the center was 30 L/min.

For the oxidation of TiC in Ar–He–O₂ plasma, the oxygen gas was injected at the tail position of the Ar–He plasma. The Ar–He plasma was composed of inert gases, and helium addition increased the thermal conductivity of the plasma. This design promoted a very short oxidation reaction localized at the plasma tail, greatly reducing the grain size of the TiO₂ and changing its phase composition.

For the oxidation of TiC in Ar–H₂–CO₂ plasma, carbon dioxide was mixed with argon and injected as the carrier gas to feed the powder; it was inputted from the plasma top to the center of the induction coils. Of the plasmas used, Ar–H₂ plasma has the highest thermal conductivity. The CO₂ decomposed at plasma temperatures above 5000 K, forming oxygen atoms and carbon monoxide. The flow rates of the carrier gas (CO₂ + Ar) were (i) $\Phi_{\text{CO}_2} = 0.5$ L/min and $\Phi_{\text{Ar}} = 4.5$ L/min, and (ii) $\Phi_{\text{CO}_2} = 0.5$ L/min and $\Phi_{\text{Ar}} = 9.5$ L/min. The higher plasma operating power, 40 kW, was used to maintain the H₂ and CO₂ containing plasma, which dissipates more energy than the other plasmas.

Characterization. The synthesized oxides were collected from the reactor walls and filters. The as-oxidized powders that formed on the reactor walls were a mixture of nanosized powders condensed from vapors and larger particles of several or several tens of micrometers solidified from oxidized liquid by in situ oxidation of the parent TiC particles. The nanosized powders were separated from the as-oxidized powders by a sedimentation treatment using ethanol solvents, which was performed by decanting the sediment of the larger particles and drying the stable dispersion at room temperature to obtain the nanoparticles. The separated nanopowders were characterized in terms of their microstructures and phase compositions by X-ray diffractometry (XRD), transmission electron microscopy (TEM), and Raman spectroscopy. The XRD used Cu K α radiation. The TEM was performed on a JEM-1010 microscope (JEOL, Akishima, Tokyo) with an accelerating voltage of 100 kV. The TEM samples were prepared by dipping ultrasonically dispersed powder samples in ethanol on copper grids. The HRTEM observations were performed on a JEM-4000EX microscope (JEOL). The Raman spectral analysis was performed on a Raman spectroscope (NR-1800, JASCO, Tokyo) with Ar⁺ laser excitation.

Results and Discussion

Powder Formation Characteristics. Our previous work showed that as TiC micropowder is fed into Ar–O₂ thermal plasma, with a moderate oxygen input in the plasma sheath gas (<10 L/min), the TiC is oxidized rapidly, predominately by a liquid or solid mechanism.³⁶ This leads to the formation of monodispersed spherical particles of TiO₂ and micrometer-size composites due to in situ oxidation of the individual TiC particles. In that case, the as-oxidized TiO₂ droplets evaporate only to a limited extent. We have now determined that when the oxygen input is increased to a much higher level, the as-oxidized products vaporize as soon as they form, resulting in predominately nanosized TiO₂ particles.

The products of the oxidized powders deposited on or at the reactor walls, on the base, and in the filter. The products were collected separately from the different locations with each part

TABLE 1: Plasma-Generation and Powder-Feeding Conditions

| | Ar–O ₂ plasma treatment | Ar–He–O ₂ plasma treatment | Ar–H ₂ –CO ₂ plasma treatment |
|----------------------------------|---|---------------------------------------|---|
| central gas and flow rate | argon, 30 L/min | argon, 30 L/min | argon, 30 L/min |
| sheath gas and flow rate | argon, 87.5, 85, 82.5, 80, 75, 70 L/min + oxygen, 2.5, 5, 7.5, 10, 15, 20 L/min | argon, 85 L/min + helium, 5 L/min | argon, 80 L/min + hydrogen, 10 L/min |
| carrier gas and flow Rate | argon, 2.5, 5, 10 L/min | argon, 5, 10 L/min | argon, 4.5, 9.5 L/min + carbon dioxide, 0.5 L/min |
| tail injection gas and flow rate | | oxygen, 5, 10 L/min | |
| RF power | 25 kW | 25 kW | 40 kW |
| chamber pressure | 53.3, 66.7, and 80.0 kPa | | |
| powder feeding rate | 1.6–1.8 g/min | | |

of the products processed by sedimentation–separation and weighted. The results showed that the amount of the local products and the fractions of the nanosize particles change with synthesis conditions, especially with the oxygen flow rate (Φ_{O_2}) in the plasma sheath gases and the carrier flow rate (Φ_C). Under typical conditions ($\Phi_{O_2} = 15$ L/min and $\Phi_C = 5$ L/min), the weight fractions for the powders collected from walls, base, and filters were 58%, 4%, and 38%, respectively, and the sedimentation separation showed that 97 wt. % of the wall-powders were nanosize particles with only 3 wt % of large particles. The filter powders occupying 38 wt. % of the total products were all nanosize products, while the base products consisted mainly (~ 80 wt. %) incompletely oxidized larger-size TiC or TiO₂/TiC powders. The overall fraction of the nanosize TiO₂ powders in the oxidized products was 93%.

The pure nanosize powder obtained in the filter resulted because the particles were carried by the gas stream after they were formed in the high-temperature zone, and they were transported to the side way of the reactor and deposited in the filter. This is in contrast to the larger, incompletely oxidized TiC particles that gained a higher acceleration and were trapped in the base of the reactor. Therefore, the different products tended to separate after the dynamic oxidation reactions.

We have noted that the ratio of the TiO₂ powders collected from the synthesis to the input TiC was 1.14 (i.e., > 1), indicating a weight increase due to oxidation. This value, however, is slightly smaller than the weight increase of 1.333 calculated from the reaction $TiC(s) + (3/2)O_2 = (TiO_2(s) + CO(g))$, which is probably due to collection loss (collection yield: ~ 86 wt. %). Assuming a 100% collection, the production rate is 2.0–2.2 g/min based on the powder input rate of 1.6–1.8 g/min.

The oxidation occurred by vaporization of TiC particles followed by instant oxidation to TiO₂. The vaporization rate R increases with the decreases of particle size d by $R \sim 1/d^2$. The oxidation reaction of TiC to TiO₂ is strongly exothermic; that also impeded the oxidation reactions in the front of the oxidation in the TiC particles.^{36,37} This causes the complete oxidation of TiC powders to TiO₂ powders. Oxidation of TiC does occur in the liquid phase that gives the TiO₂ particles, or the TiO₂/TiC core–shell particles of sizes at the similar scale as the starting TiC particles. This was observed at a lower oxygen concentration that is not the major process under the present experimental conditions.

The color of the oxide powders distinctly changed with the synthesis conditions (Figure 2). It changed from gray to white with increasing oxygen flow rate in the Ar–O₂ plasma. The powders formed in the Ar–He–O₂ plasma with tail oxygen injection and in the Ar–H₂–CO₂ plasma were consistently gray, irrespective of the gaseous concentration. The different colors reflect the different phase compositions and stoichiometries of the powders formed under the different conditions. Because pure rutile and anatase have a wide band gap (3.2 eV), they should be transparent to visible light and colorless.⁴² However, when the oxygen content of rutile is slightly reduced, it takes on a

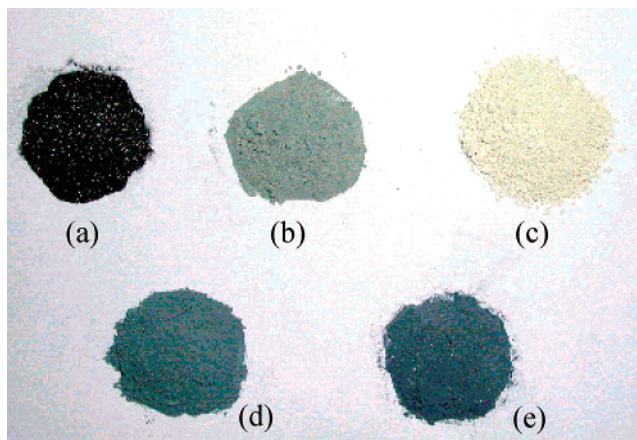


Figure 2. Appearance of nanocrystalline TiO₂ powders synthesized by plasma oxidation showing different colors: (a) starting TiC micrometer-size powder; nanocrystalline TiO₂ powder (b) synthesized in Ar–O₂ plasma at $\Phi_{O_2} = 7.5$ L/min, (c) in Ar–O₂ plasma at $\Phi_{O_2} = 15$ L/min, (d) in Ar–He–O₂ plasma with tail oxygen injection at $\Phi_{O_2} = 10$ L/min, and (e) in Ar–H₂–CO₂ plasma at $\Phi_{CO_2} = 0.5$ L/min and $\Phi_C = 5$ L/min.

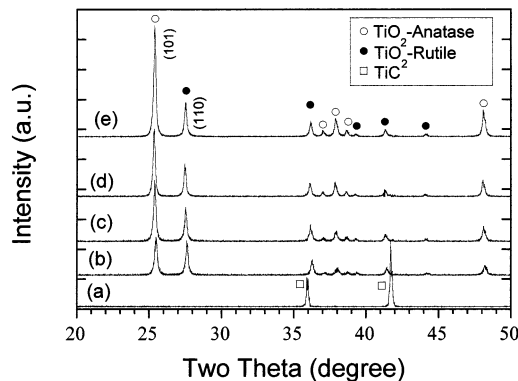


Figure 3. X-ray diffraction results of TiO₂ nanocrystallites in Ar–O₂ plasma at different oxygen flow rates: (a) starting TiC powders; (b)–(e) $\Phi_{O_2} = 5, 10, 15$, and 20 , respectively.

blue tint, which deepens to purple and black with increasing oxygen deficiency.⁴³ The deep color of the present powders suggests the formation of defective rutile due to an oxygen deficiency and that the deepness of color increase with the increase in oxygen deficiency. The coloration is very sensitive to changes in the nonstoichiometry of TiO_{2-x}, although the oxygen deficiency is at most 0.01 in the tetragonal rutile structure.⁴⁴

Phase Formation under Different Conditions. Figure 3 shows XRD results for TiO₂ nanopowders obtained at different oxygen flow rates in Ar–O₂ plasma. The powders were nanosize and consisted of anatase and rutile. No residue TiC was found in them. The intensities of the diffraction lines for the anatase increased steadily with the oxygen flow rate. The weight fractions were calculated from the relative intensities of the

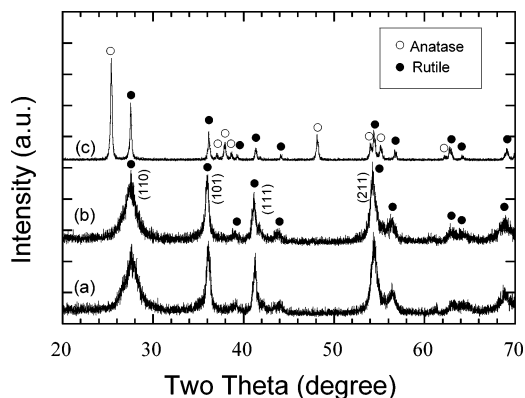


Figure 4. X-ray diffraction results of TiO₂ synthesized in Ar-H₂-CO₂ plasma at two different total carrier flow rates, Φ_C : (a) $\Phi_{CO_2} = 0.5$ L/min, $\Phi_C = 5$ L/min, and (b) $\Phi_{CO_2} = 0.5$ L/min, $\Phi_C = 10$ L/min, in comparison with (c) TiO₂ synthesized in Ar-O₂ plasma at $\Phi_{O_2} = 10$ L/min, $\Phi_C = 5$ L/min.

strongest peaks for anatase (101) and rutile (110) based on the relationship established by Spurr and Myers, $\{[\text{anatase}]/[\text{rutile}]\} = 0.79[(I_A(101)/I_R(110))]$.⁴⁵ The percentages of anatase formed at $\Phi_{O_2} = 5, 10, 15,$ and 20 L/min were 46, 58, 64, and 75 wt. %, respectively. The increase in the metastable anatase phase content in nanocrystallites with the oxygen flow rate agrees with the phase selection during homogeneous nucleation in considerably undercooled melt.⁴⁶ Increasing the oxygen flow rate increases the thermal conductivity of the plasma slightly, which increases the plasma cooling rate and the degree of the undercooling stream, where the nucleation in the gas phase and the subsequent growth of particles occur.

Figure 4 shows the XRD results for TiO₂ nanocrystallites synthesized in Ar-H₂-CO₂ plasma at $\Phi_{CO_2} = 0.5$ L/min with a total carrier flow rate of $\Phi_C = 5$ or 10 L/min, compared with those for Ar-O₂ plasma at $\Phi_{O_2} = 10$ L/min with $\Phi_C = 5$ L/min. Note that the phase formed in the Ar-H₂-CO₂ plasma was exclusively rutile, irrespective of the carrier gas flow rate. The diffraction lines of rutile formed in the Ar-H₂-CO₂ plasma broadened considerably compared with those formed in the Ar-O₂ plasma, suggesting significantly reduced grain sizes. The mean grain sizes of rutile formed in the Ar-H₂-CO₂ plasma were estimated from the diffraction line broadening using the Scherrer Equation ($D = 0.89\lambda/\beta\cos\theta$)⁴⁷ to be 10 and 12 nm at $\Phi_C = 5$ and 10 L/min, respectively, considerably less than the 92 nm for rutile formed at $\Phi_{O_2} = 10$ L/min in Ar-O₂ plasma. Thus, very small pure rutile nanocrystallites can be obtained by oxidation of TiC in Ar-H₂-CO₂ plasma.

The structures of the two modifications of TiO₂ (rutile and anatase) were very sensitive to Raman scattering, which can provide valuable information about the phase compositions and quality of crystallinity as well as crystal sizes. Figure 5 shows the Raman spectra of powders synthesized at different oxygen flow rates in Ar-O₂ plasma. Those obtained at $\Phi_{O_2} > 10$ L/min exhibited three Raman bands at 144, 393, and 635 cm⁻¹ corresponding to the E_g, B_{1g}, and E_g modes for anatase.⁴⁸ The sharp Raman bands indicate that the nanocrystalline anatase was of high quality. The increase in intensity of these bands with the oxygen flow rate is in agreement with the XRD results (Figure 3). In addition, no Raman bands were detected in the vicinity of 1350 or 1500 cm⁻¹, providing clear evidence of the absence of any amorphous carbon or graphite in the synthesized oxides.

The spectrum for $\Phi_{O_2} = 5$ L/min (Figure 5) features two broad bands in the ranges 360–460 and 590–660 cm⁻¹, which

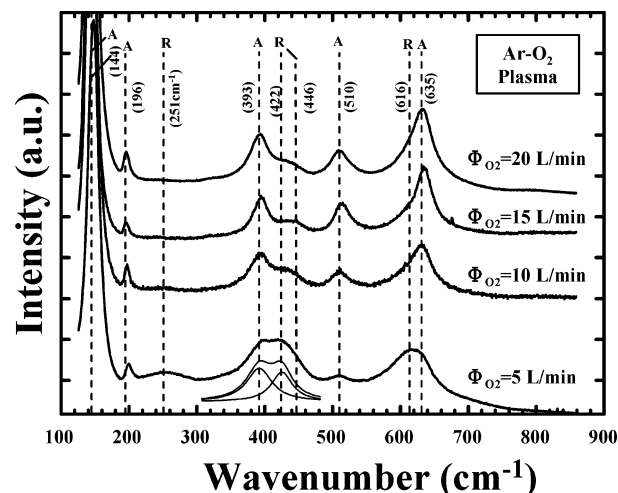


Figure 5. Raman spectra of TiO₂ nanocrystallites synthesized in Ar-O₂ plasma ($\Phi_C = 5$ L/min) at different oxygen flow rates; $\Phi_{O_2} = 5, 10, 15, 20$ L/min.

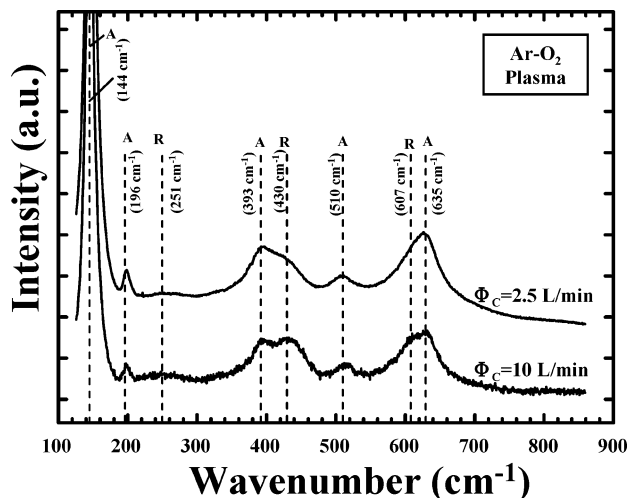


Figure 6. Raman spectra of TiO₂ nanocrystallites synthesized in Ar-O₂ plasma ($\Phi_{O_2} = 5$ L/min) at different carrier flow rates, Φ_C : (a) 2.5 and (b) 10 L/min.

are apparently an overlap of the Raman bands for anatase and rutile near these regions. The rutile band at 422 cm⁻¹ was red-shifted by 24 cm⁻¹ from the E_g mode at 446 cm⁻¹ for stoichiometric rutile TiO₂.⁴³ This red shift was observed in nanophase TiO₂ prepared using a gas condensation method under high vacuum conditions,⁴⁹ indicating that the red shift was due to oxygen deficiency in the TiO₂. This large red shift was also probably caused by the defective structure of the rutile formed when the oxygen input was low. The gray color of the powders formed under these conditions also suggests an oxygen-reduced rutile structure. No such Raman-band shift was observed for the rutile phase formed at $\Phi_{O_2} = 15$ or 20 L/min, indicating that stoichiometric rutile with an ideal structure is formed at high oxygen concentrations, as also indicated by the white color of the powders formed under such conditions. These results show that the oxygen concentration affects not only the phase content, but also the structure of rutile.

Besides the oxygen input, the flow rate of the carrier gas for powder feeding (Φ_C) was found to have a pronounced effect on phase formation. Figures 6 and 7 show the Raman spectra of TiO₂ nanopowders formed at different values of Φ_C in Ar-O₂ plasma and in Ar-He plasma with tail oxygen injection, respectively. In both cases, a lower Φ_C (2.5 L/min) promoted

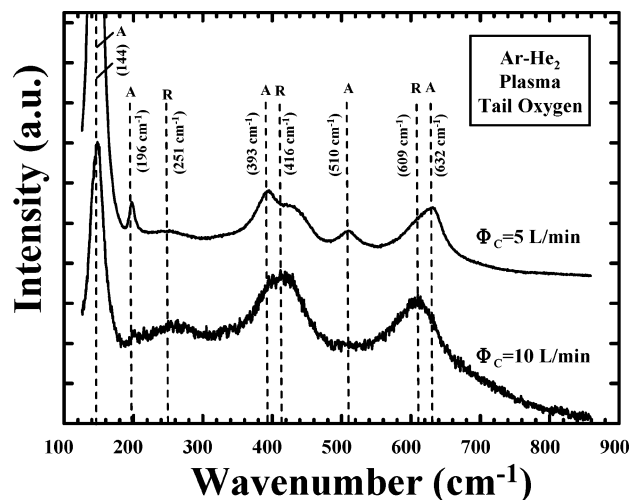


Figure 7. Raman spectra of TiO₂ nanopowders synthesized in Ar–He plasma with tail oxygen injection ($\Phi_{O_2} = 5$ L/min) at different carrier flow rates, Φ_C : (a) 5 and (b) 10 L/min.

the formation of anatase, while a higher Φ_C (10 L/min) promoted the formation of rutile. Again, there was a considerable red shift of the E_g mode of rutile (as large as 35 cm^{-1}), suggesting that a significantly defective rutile structure formed under these conditions. The oxide formed at $\Phi_C = 10$ L/min with tail injection consisted mainly of rutile (92 wt. %), so the tail injection configuration provides an alternative for obtaining rutile nanocrystallites.

Summarizing the role of phase formation in the plasma oxidation process, the results described above demonstrate (i) that rutile nanocrystallites were formed in Ar–H₂–CO₂ plasma and in Ar–O₂ plasma at higher carrier flow rates and (ii) that anatase and rutile nanocrystallites with different ratios were formed in Ar–O₂ plasma, and the phase content depended on the oxygen concentration in the reaction system. Note that 100% rutile was formed in Ar–H₂–CO₂ plasma, regardless of the concentration of CO₂ in the system. A thermodynamic calculation showed that, in the Ar–H₂–CO₂ system, only a low concentration of oxygen atoms formed through the dissociation of CO₂ at temperatures above 5000 K. Pure rutile nanocrystallites were also observed in in-flight Ar–H₂–O₂ thermal plasma oxidation of micro-sized TiN powder.⁵⁰ This indicates that a relatively low oxygen pressure in plasma may play a key role in the growth of oxygen-deficient rutile nanocrystallites. Rutile with a weight fraction > 92 wt. % was formed in the Ar–O₂ plasma at a higher carrier flow rate. The enhanced formation of rutile rather than anatase with the increased velocity of oxidizing particles (hence a higher cooling rate) is somewhat surprising because rutile is thermodynamically more stable than anatase, and the anatase phase should be preferably formed in supercooled melt.⁴⁶ This can be explained as follows: at a higher velocity, the residence time of TiC particles in the higher oxygen concentration region was shorter, and oxidation took longer in the dilute oxygen region (lower oxygen concentration), promoting the formation of rutile with an oxygen-reduced structure (defective rutile structure).

Morphology and Microstructures. TEM images of nanocrystalline TiO₂ formed in Ar–O₂ and Ar–He–O₂ plasmas are shown in Figure 8. The nanocrystalline TiO₂ that formed in the Ar–O₂ plasma consisted of monodispersed spherical and faceted particles with a typically hexagonal morphology. The particle size (grain size) was 20–100 nm. The electron diffraction patterns revealed a set of polycrystalline diffraction rings corresponding to the rutile and anatase structures. In contrast,

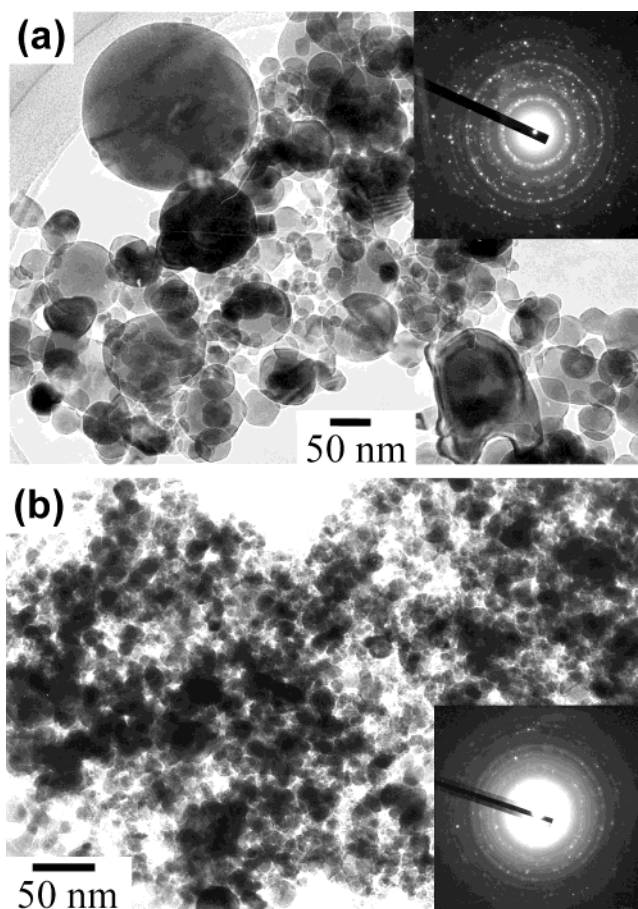


Figure 8. TEM images of TiO₂ nanocrystallites synthesized in (a) Ar–O₂ plasma and (b) Ar–He–O₂ plasma with tail oxygen injection. Flow rates of oxygen were the same in both cases, $\Phi_{O_2} = 10$ L/min.

the particles formed in the Ar–He–O₂ plasma via tail oxygen injection were much smaller, below 15 nm, and more uniform. The corresponding electron diffraction patterns featured a set of faint thick rings due to the decreased grain sizes. The sizes of the TiO₂ nanocrystallites can thus be changed greatly by injecting oxygen at different locations in the plasma. The reduced sizes for the tail injection were simply due to the reduced time for particle growth by vapor condensation.

The nanocrystalline TiO₂ that formed in the Ar–O₂ plasma was characterized by single-crystal structures, as revealed by HRTEM. Figure 9a1 shows a hexagonal particle 15 nm in diameter; its single-crystal structure has a high degree of crystallinity. The space between the lattice planes (Figure 9a2) was 0.246 nm, which corresponds well to the d value of (101) planes for rutile. The surface of the particle had an amorphous layer 0.5–1.0 nm thick. Figure 9b1 shows a spherical particle from the same product batch. The lattice spacing of 0.352 nm (Figure 9b2) is equal to the d value of (101) planes for anatase. An amorphous dislocation region was observed at the periphery of this particle (the arrowed region); it is the grain boundary formed due to incomplete coagulation during particle growth. We found that most of the rutile particles crystallized into hexagonal shapes while the anatase ones crystallized into spherical shapes.

Figure 10 shows an HRTEM image of TiO₂ nanocrystallites formed in Ar–He–O₂ plasma with tail oxygen injection. As expected, the grain size was much smaller than with top injection (Figure 8), which was around 10 nm. The particles appeared as either single crystals or polycrystallites. The crystalline quality was lower than for top injection. Most of the particles contained

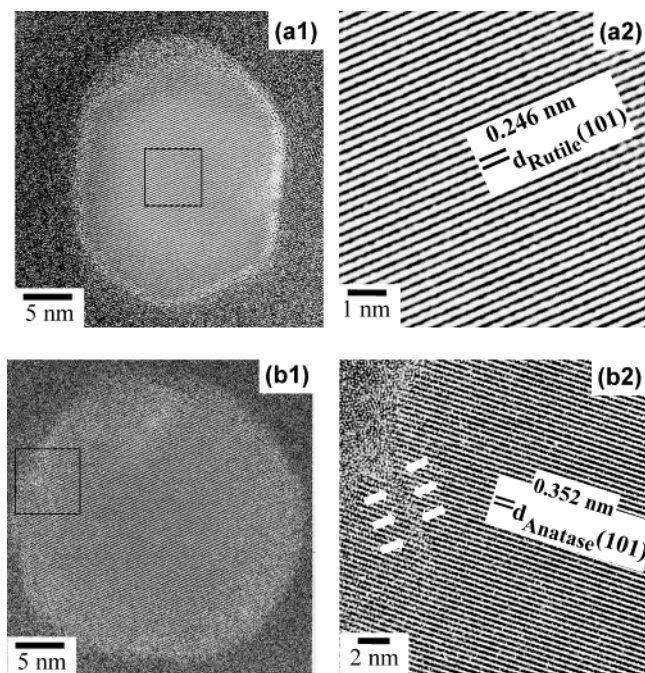


Figure 9. HRTEM images of cross-sections of TiO₂ nanocrystallites synthesized in Ar–O₂ plasma at $\Phi_{O_2} = 15$ L/min showing (a) hexagonal rutile single crystal and (b) anatase single crystal with a spherical shape.

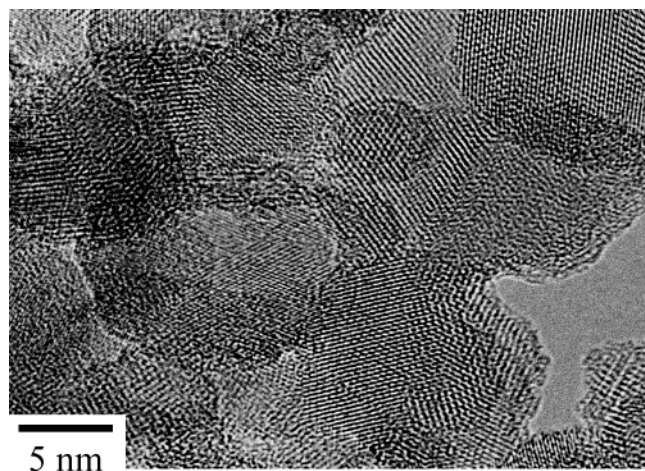


Figure 10. HRTEM image of TiO₂ nanocrystallites synthesized in Ar–He plasma with tail oxygen injection at $\Phi_{O_2} = 10$ L/min.

extensive linear dislocations, lattice distortions, and/or domains, resulting from incomplete crystallization or sintering of the primary grains in association with the increased cooling rate.

The morphology and TEM and HRTEM images of nanocrystalline TiO₂ synthesized in Ar–H₂–CO₂ plasma are shown in Figures 11a and b. As shown already by XRD (Figure 3), the TiO₂ powder formed under these conditions was completely rutile. The TEM image shows that the particles did not agglomerate and that the particle size was around 30 nm. The rutile structure of the particles was further confirmed by electron diffraction (insert). Note that most of the particles appeared as faceted grains rather than as regular hexagonal ones. Densely distributed layer dislocations in the grains are discernible in the image. This structural characteristic is apparently related to the defective rutile structure (with an oxygen deficiency) that formed under these conditions, which altered the densely arranged lattice plane in the tetragonal structure of the crystals.

The nanocrystallites in the present work exhibited the same phase selection as ones synthesized through in-flight thermal-

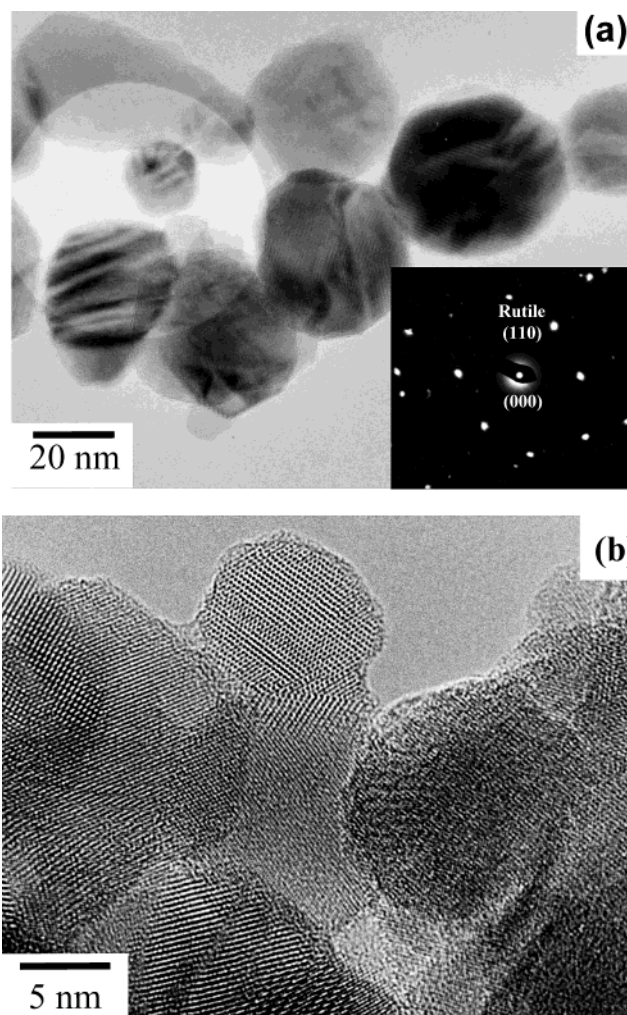


Figure 11. (a) TEM and (b) HRTEM images of TiO₂ nanocrystallites synthesized in Ar–H₂–CO₂ plasma at $\Phi_{CO_2} = 0.5$ L/min and $\Phi_C = 10$ L/min.

plasma oxidation of TiN powder.⁵⁰ The photocatalytic property of the latter appears in the visual light region due to the appreciable amount of nitrogen incorporated into the powder, whereas that of our nanocrystallites appeared only with UV light irradiation. We are now investigating the photoluminescence of TiO₂ nanocrystallites.

Conclusion

Nanocrystalline TiO₂ with particle sizes of 10–50 nm was produced efficiently by thermal plasma oxidation of titanium carbide in an aerosol flowing reactor. This novel process enabled the controlled formation of anatase and rutile; the grain sizes were controlled by performing the reaction in different plasma gases (Ar–O₂ or Ar–H₂–CO₂) or by injecting oxygen at different locations in the reaction system. The reduced concentration of oxygen atoms in the gas phase promoted the preferable formation of rutile. Pure rutile nanocrystallites (10–15 nm in size) were produced by oxidizing TiC in Ar–H₂–CO₂ plasma. Synthesis in Ar–O₂ plasma produced a mixture of monodispersed hexagonal rutile and spherical anatase grains (20–50 nm in size). The anatase/rutile ratio was controlled simply by adjusting the oxygen input in the plasma sheath gas (Ar + O₂) and it varied from 20 to 75 wt. %. The variation probably came from the temperature variation history during the nucleation and the following growth. The rapid cooling suppressed the supply of oxygen into the coagulated particles, promoting the formation

of oxygen-deficient rutile. The flow rate of the carrier gas for the powder feeding was adjusted to control the phase composition; the composition was >90 wt. % rutile at higher carrier flow rates. Moreover, injecting oxygen at the tail of the Ar–He plasma greatly reduced the grain size compared to using top injection. The grain size was more precisely controlled by selectively injecting the oxygen at various locations in the plasma. The present work distinctly showed the importance of controlling the reaction atmosphere as well as the thermal history in the synthesis of TiO₂ nanocrystallites.

Acknowledgment. We greatly thank Dr. Kenji Watanabe and Dr. Seung-Min Oh of NIMS for their input on Raman spectroscopy and plasma-synthesized TiO₂, respectively.

References and Notes

- (1) Schiavello, M. *Photocatalysis and Environment. Trends and Applications*; NATO ASI Series; Kluwer Academic Publishers: Dordrecht, 1988.
- (2) Bahnmann, D. W.; Kholuiskaya, S. N.; Dillert, R.; Kulak, A. I.; Kokorin, A. I. *Appl. Catal., B* **2002**, 36 (2), 161.
- (3) Tomkiewicz, M. *Catal. Today* **2000**, 58 (2–3), 115.
- (4) Gratzel, M. *Nature* **2001**, 414, 338.
- (5) Nazeeruddin, M. K.; Pechy, P.; Renouard, T.; Zakeeruddin, S. M.; Humphry-Baker, R.; Comte, P.; Liska, P.; Cevey, L.; Costa, E.; Shklover, V.; Spiccia, L.; Deacon, G. B.; Bignozzi, C. A.; Gratzel, M. *J. Am. Chem. Soc.* **2001**, 123 (8), 1613.
- (6) Flood, R. U.; Fitzmaurice, D. *J. Phys. Chem.* **1995**, 99 (22), 8954.
- (7) Sotomayor, J.; Hoyle, R. W.; Will, G.; Fitzmaurice, D. *J. Mater. Chem.* **1998**, 8 (1), 105.
- (8) Lin, H. M.; Keng, C. H.; Tung, C. Y. *Nanostruct. Mater.* **1997**, 9 (1–8), 747.
- (9) Bhowmik, S.; Constant, K. P.; Parker, J. C.; Ali, M. *Mater. Sci. Eng.* **1995**, 204 (1–2), 258.
- (10) Kumar, K. P.; Keizer, K.; Burggraaf, A. J.; Okubo, T.; Nagamoto, H.; Morooka, S. *Nature* **1992**, 358, 48.
- (11) Siegel, R. W. *Mater. Sci. Eng., B* **1993**, 19 (1–2), 37.
- (12) Ollis, D. F.; Al-Ekabi, H. *Photocatalytic Purification and Treatment of Water and Air*; Elsevier: Amsterdam, 1993.
- (13) Hamerski, M.; Grzechulska, J.; Morawski, A. W. *Solar Energy* **1999**, 66 (6), 395.
- (14) Seo, D. S.; Lee, J. K.; Kim, H. *J. Cryst. Growth* **2001**, 233, 298.
- (15) Guan, Z. S.; Zhang, X. T.; Ma, Y.; Cao, Y. A.; Yao, J. N. *J. Mater. Res.* **2001**, 16 (4), 907.
- (16) Zhang, Q.; Gao, L.; Guo, J. *J. Eur. Ceram. Soc.* **2000**, 20, 2153.
- (17) Trentler, T. J.; Denler, T. E.; Bertone, J. F.; Agrawal, A.; Colvin, V. L. *J. Am. Ceram. Soc.* **1999**, 121, 1613.
- (18) Ahonen, P. P.; Kauppinen, E. I.; Joubert, J. C.; Deschamps, J. L.; Van Tendeloo, G. *J. Mater. Res.* **1999**, 14 (10), 3938.
- (19) Kasuga, T.; Hiramatsu, M.; Hirano, M.; Hosono, A.; Oyama, K. *J. Mater. Res.* **1997**, 12 (3), 607.
- (20) Shklover, V.; Nazeeruddin, M. K.; Zakeeruddin, S. M.; Barbe, C.; Kay, A.; Haibach, T.; Steurer, W.; Hermann, R.; Nissen, H. U.; Gratzel, M. *Chem. Mater.* **1997**, 9, 430.
- (21) Chan, C. K.; Porter, J. F.; Li, Y. G.; Guo, W.; Chan, C. M. *J. Am. Ceram. Soc.* **1999**, 82 (3), 566.
- (22) Zhang, Z. B.; Wang, C. C.; Zakaria, R.; Ying, J. Y. *J. Phys. Chem. B* **1998**, 102 (52), 10871.
- (23) Zhang, Q. H.; Gao, L.; Zheng, S. *Acta Chim. Sinica* **2001**, 9 (11), 1909.
- (24) Gao, L.; Zhang, Q. *Script. Mater.* **2001**, 44, 1195.
- (25) Rivera, A. P.; Tanaka, K.; Hisanaga, T. *Appl. Catal., B* **1993**, 3, 37.
- (26) Pratsinis, S. E.; Vemury, S. *Powder Technol.* **1996**, 88, 267.
- (27) Pratsinis, S. E. *Powder Technol.* **1996**, 86, 87.
- (28) Akhtar, M. K.; Pratsinis, S. E. *J. Am. Ceram. Soc.* **1992**, 75 (12), 3408.
- (29) Skandan, G.; Chen, Y. J.; Glumac, N.; Kear, B. H. *Nanostruct. Mater.* **1999**, 11 (2), 149.
- (30) Ding, X. Z.; Liu, X. H.; He, Y. Z. *J. Mater. Sci. Lett.* **1996**, 15, 1789.
- (31) Ding, X. Z.; Liu, X. H. *J. Mater. Res.* **1998**, 13 (9), 2556.
- (32) Eastman, J. A. *J. Appl. Phys.* **1994**, 75 (2), 770.
- (33) Bacsa, R. R.; Gratzel, M. *J. Am. Ceram. Soc.* **1996**, 79 (8), 2185.
- (34) Wang, C. C.; Ying, J. Y. *Chem. Mater.* **1999**, 11, 3113.
- (35) Ovenstone, J.; Yanagisawa, K. *Chem. Mater.* **1999**, 11, 2770.
- (36) Li, Y.; Ishigaki, T. *J. Am. Ceram. Soc.* **2001**, 84 (9), 1929.
- (37) Young, R. M.; Pfender, E. *Plasma Chem. Plasma Process* **1985**, 5 (1), 1.
- (38) Li, Y.; Ishigaki, T. *Chem. Mater.* **2001**, 13 (5), 1577.
- (39) Ishigaki, T.; Li, Y.; Kataoka, E. *J. Am. Ceram. Soc.* **2003**, 86 (9), 1456.
- (40) Li, Y.; Ishigaki, T. *Chem. Phys. Lett.* **2003**, 367 (5–6), 561.
- (41) Fan, X.; Ishigaki, T.; Suetsugu, Y.; Tanaka, J.; Sato, Y. *J. Am. Ceram. Soc.* **1998**, 81 (10), 2517.
- (42) Elder, S. H.; Cot, F. M.; Su, Y.; Heald, S. M.; Tyryshkin, A. M.; Bowman, M. K.; Gao, Y.; Joly, A. G.; Balmer, M. L.; Kolwaite, A. C.; Magrini, K. A.; Blake, D. M. *J. Am. Chem. Soc.* **2000**, 122, 5138.
- (43) Betsch, R. J.; Park, H. L.; White, W. B. *Mater. Res. Bull.* **1991**, 26, 613.
- (44) Kofstad, P. *Nonstoichiometry, Diffusion, and Electrical Conductivity in Binary Metal Oxides*; John Wiley: New York, 1972; p 139.
- (45) Spurr, R. A.; Myers, H. *Anal. Chem.* **1957**, 29 (5), 760.
- (46) Li, Y.; Ishigaki, T. *J. Cryst. Growth* **2002**, 242 (3/4), 511.
- (47) Klug, H. P.; Alexander, L. E. *X-ray Diffraction Procedure of Polycrystalline and Amorphous Materials*; John Wiley: New York, 1954; p 495.
- (48) Ohsaka, T.; Izumi, F.; Fujiki, Y. *J. Raman Spectrosc.* **1978**, 7, 321.
- (49) Parker, J. C.; Siegel, R. W. *J. Mater. Res.* **1990**, 5 (6), 1246.
- (50) Oh, S.; Ishigaki, T. *Thin Solid Films* **2004**, 457 (1), 186.